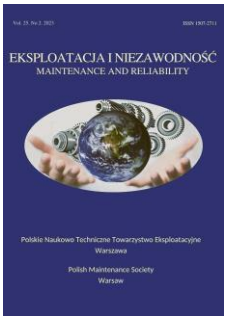

Eksploatacja i Niezawodnosc – Maintenance and Reliability
Volume 28 (2026), Issue 3
journal homepage: http://www.ein.org.pl

Article citation info:
Li K, Zhang F, Sun X, Wang J, An Explainable and Adaptive Anomaly Detection Method for Multi-Condition Monitoring of Intelligent Equipment, Eksploatacja i Niezawodnosc – Maintenance and Reliability 2026: 28(3) http://doi.org/10.17531/ein/218122

An Explainable and Adaptive Anomaly Detection Method for Multi-Condition Monitoring of Intelligent Equipment

Indexed by: Web of Science Group

Kaiping Li[a,b], Fengli Zhang[a,b,*], Xuehao Sun[a,b], Jinjiang Wang[a,b]

[a] School of Mechanical and Transportation Engineering, China University of Petroleum, Beijing 102249, China
[b] Key Laboratory of Oil and Gas Production Equipment Quality Inspection and Health Diagnosis, State Administration for Market Regulation, Beijing 102249, China

Highlights

- Constructing a spatial memory matrix via improved K-Nearest Neighbors and K-means.
- A weighted MSET-SPRT hybrid model is proposed to enable state-adaptive residual evaluation.
- Proposed an interpretability framework quantifying parameter-wise residual contributions.

Abstract

This paper addresses the challenges of weak parameter correlation, low detection accuracy, and poor interpretability in anomaly detection for rotating machinery under multi-condition operating scenarios. An explainable adaptive anomaly detection method is proposed. First, sensitivity and correlation analyses are employed to optimize the input parameters, and a spatial memory matrix is constructed by integrating an improved K-Nearest Neighbors algorithm with K-means clustering. Second, a multi-parameter anomaly detection model based on multivariate state estimation technique and sequential probability ratio test is developed to enable adaptive diagnosis of equipment operating conditions. Finally, error statistics are used to model the contribution trajectories of anomalous parameters, combined with a cumulative anomaly contribution rate metric to enhance the interpretability of anomaly localization. Experimental results show that the proposed method attains an average accuracy of 97.47% on multi-condition datasets, underscoring its wide applicability in industrial equipment monitoring.

Keywords
explainable adaptive anomaly detection, sensitivity and correlation analyses, spatial memory matrix, multivariate state estimation technique, sequential probability ratio test

1. Introduction

Rotating machinery is widely used in large-scale engineering fields such as aerospace, railway transportation, and energy exploration [1,2]. During operation, these machines are often subjected to harsh operating conditions, such as high speeds and heavy loads, which pose significant challenges to performance stability and production continuity. As a critical precision support component of rotating machinery, the operating condition of rolling bearings has a decisive impact on equipment accuracy and reliability [3–5]. Once a failure occurs, it can lead to a significant increase in operation and maintenance costs, and in severe cases, may even jeopardize personnel safety [6–8]. Therefore, research on fault prediction and health management (PHM) for rotating machinery is of utmost importance. Anomaly detection, as a key part of PHM, analyzes multidimensional historical data generated by the equipment to achieve accurate monitoring and assessment of the current condition, significantly improving maintenance efficiency and overall reliability.

Currently, Anomaly detection methods are typically classified into supervised, semi-supervised, and unsupervised

(*) Corresponding author.
E-mail addresses: K. Li (ORCID: 0009-0003-3854-5380) 1425709546@qq.com, F. Zhang (ORCID: 0000-0003-0720-8202) fengliz14@163.com, X. Sun (ORCID: 0000-0002-5856-6037) easysxh@163.com, J. Wang (ORCID: 0000-0003-0163-4446) jwang@cup.edu.cn

learning based on data labels [9]. Due to limited labeled fault data in operational environments, unsupervised learning, has become the mainstream approach.Wang et al. [10] used the 3-sigma rule to set degradation thresholds, enabling precise detection of bearing degradation onset. Hardin et al. [11] combined the Minimum Covariance Determinant estimate with the Minimum Standard Deviation method to calculate robust threshold distances, and used F-distribution model to identify outliers in the case of multiple clusters. However, traditional univariate methods face limitations such as underutilization of equipment data and biased status evaluations, compromising detection accuracy and reliability.

To overcome the limitations of univariate methods, researchers have gradually explored multivariate detection to achieve more comprehensive and effective anomaly detection. The Multivariate State Estimation Technique (MSET) offers distinct advantages as it requires no complex model training, while maintaining low computational costs, procedural simplicity, and strong generalization capabilities [12]. Guo et al. [13] applied adaptive MSET for early fault detection in induced draft fans at power plants, enhancing generalization. Caesarendra et al. [14] used MSET with kernel regression for defect detection and remaining life prediction in low-speed slewing bearings.

Recently, machine learning methods, including linear, proximity-based, and ensemble-based techniques, have been increasingly applied to anomaly detection in rotating equipment [15]. Principal Component Analysis (PCA) and One-Class Support Vector Machine (OC-SVM) are typical linear methods. Yang et al. [16] used PCA for marine turbine generators, combining Hotelling's T2 and Q statistics to improve fault detection accuracy. Saari et al. [17] developed an OC-SVM-based fault detection model for wind turbines, demonstrating superior speed and accuracy compared to traditional methods. Among unsupervised detection approaches, proximity-based anomaly detection methods encompasses clustering, distance, and density. Wang et al. [18] improved wind turbine anomaly detection by enhancing density-based spatial clustering, addressing noise sensitivity. Cui et al. [19] achieved high satellite anomaly detection accuracy using Fast Dynamic Time Warping and K-Nearest Neighbors (KNN). Wang et al. [20] proposed the Dynamic Adaptive Local Outlier Factor (DALOF) method to improve rotating machinery detection. The anomaly detection methods based on ensemble learning are mainly represented by the Isolation Forest(IF). Shu et al. [21] combined random convolution kernels with IF, showing superior performance on various rotating machinery datasets. Although these traditional methods have been effective in anomaly detection, they struggle to extract complex features from multivariate time-series data. As data dimensionality increases, they face the curse of dimensionality, significantly impacting real-time detection accuracy and computational efficiency.

As a core branch of machine learning, deep learning has emerged as a prominent methodology, offering significant advantages in efficiently modeling complex nonlinear and non-stationary data [22]. Li et al. [23] enhanced Computer Numerical Control machine detection accuracy using ensemble learning with Long Short-Term Memory AutoEncoders. Li et al. [24] achieved real-time nuclear plant monitoring (3 ms response) by combining variational autoencoders with IF. However, these methods often overlook inter-variable correlations and suffer from the "black box" nature of machine learning, limiting anomaly identification and reducing interpretability.

In summary, this study proposes an explainable and adaptive anomaly detection method for rotating machinery under multiple working conditions, addressing three critical limitations in existing methods: insufficient consideration of parameter correlations in complex operating environments, low anomaly detection accuracy, and ambiguous mechanisms for anomaly parameter localization. The main contributions include:

1) An input parameter selection method combining correlation and conflict indicators;
2) An improved KNN and K-means-based spatial memory matrix (MM) construction method that enhances prediction vector accuracy;
3) A weighted MSET-Sequential Probability Ratio Test (SPRT) hybrid model enabling state-adaptive residual evaluation; and
4) An interpretability framework quantifying parameter-wise residual contributions.

The remainder of the article is organized as follows. Section 2 describes methodological foundations. Section 3 presents the integrated framework. Section 4 illustrates the feasibility of the proposed method using case studies. Section 5 provides

a comprehensive discussion on the proposed method from the perspectives of model performance, interpretability, and generalizability. Section 6 concludes.

2. Theoretical basis

2.1. Weighted Nearest-Neighbor-Based MSET Method

A comprehensive dataset of historical operational records, comprising exclusively normal operating conditions, is utilized to construct a baseline health MM, $\boldsymbol{D}$, which serves as a representation of the equipment's normal state. In this matrix, each row corresponds to a monitoring parameter, with a total of i rows, i.e, $i = 1,2,\ldots,n$; each column represents the state vector at a certain time point, with a total of j columns, i.e., $j = 1,2,\ldots,m$. The structural formulation of matrix $\boldsymbol{D}$ is given by Eq. (1):

$$\boldsymbol{D} = [\boldsymbol{X}(t_1)\boldsymbol{X}(t_2)\cdots\boldsymbol{X}(t_m)] = \begin{bmatrix} x_1(t_1)x_1(t_2)\cdots x_1(t_m) \\ x_2(t_1)x_2(t_2)\cdots x_2(t_m) \\ \vdots \quad \vdots \quad \vdots \quad \vdots \\ x_n(t_1)x_n(t_2)\cdots x_n(t_m) \end{bmatrix}_{n\times m} \tag{1}$$

where $x_n(t_m)$ denotes the measured value of the monitoring parameter x_n at sampling time t_m, and $\boldsymbol{X}(t_m)$ represents the state vector at time t_m.

Given an observed state vector $\boldsymbol{X}_{obs}$ at a specific time,the estimated state vector $\boldsymbol{X}_{est}$ can be computed using the following equation.

$$\begin{aligned} \boldsymbol{X}_{\text{est}} &= \boldsymbol{D}\cdot\boldsymbol{W} = \boldsymbol{D}\cdot[w_1, w_2\cdots w_m]^T \\ &= w_1\boldsymbol{X}(t_1) + w_2\boldsymbol{X}(t_2) + \cdots + w_m\boldsymbol{X}(t_m) \end{aligned} \tag{2}$$

where the weight vector $\boldsymbol{W}$ reflects the similarity between $\boldsymbol{X}_{\text{est}}$ and each column vector in the , To further improve the estimation accuracy of the model and the robustness to outliers, the nearest neighbor weight method is used to calculate the weight coefficients, as shown in Eq. (3):

$$w_k = \frac{exp^{-||\boldsymbol{D}_k - \boldsymbol{X}_{obs}||_2}}{\sum_{j=1}^{m} exp^{-||\boldsymbol{D}_j - \boldsymbol{X}_{obs}||_2}} \tag{3}$$

Eq. (3) assigns higher weights to samples closer to the MM, enabling nonlinear weighted estimation of the observation vector. Here, $\boldsymbol{D}_k$ represents the $k-th$ column of state data.

Substituting Eq. (3) into Eq. (2), the final expression for estimating the state vector $\boldsymbol{X}_{\text{est}}$ is derived as:

$$\boldsymbol{X}_{\text{est}} = \sum_{k=1}^{m} w_k\cdot\boldsymbol{D}_k = \sum_{k=1}^{m}\left(\frac{exp^{-||\boldsymbol{D}_k - \boldsymbol{X}_{obs}||_2}}{\sum_{j=1}^{m} exp^{-||\boldsymbol{D}_j - \boldsymbol{X}_{obs}||_2}}\right)\cdot\boldsymbol{D}_k \tag{4}$$

The residual vector $\boldsymbol{e}$ is calculated using $\boldsymbol{X}_{\text{est}}$ and $\boldsymbol{X}_{obs}$:

$$\boldsymbol{e} = \boldsymbol{X}_{obs} - \boldsymbol{X}_{\text{est}} \tag{5}$$

2.2. Sequential Probability Ratio Test (SPRT)

The SPRT is a multi - stage detection method, which can track the trend of slow - growing faults. When the threshold of relevant indicators reaches the preset standard, the detection result can be obtained [25]. In this paper, the sequence vector $\boldsymbol{e} = \{e_1, e_2, \cdots, e_n\}$ is set as the residual vector between $\boldsymbol{X}_{obs}$ and $\boldsymbol{X}_{est}$, and the parameters follow a global normal distribution.

Assume the null hypothesis H_0 represents the residual distribution under a normal (healthy) condition, that is, $H_0 \sim (\mu_0, \sigma_0^2)$, and the alternative hypothesis H_1 represents the residual distribution under an abnormal condition, that is, $H_1 \sim (\mu_1, \sigma_1^2)$. During detection, the degree of dispersion is consistent, that is, ${\sigma_1}^2 = {\sigma_0}^2$ .Then, the joint probability density of n samples is:

$$P_{(H_0,n)} = \frac{1}{\left(\sigma_0\sqrt{2\pi}\right)^n}\exp\left(-\frac{1}{2\sigma_0^2}\sum_{i=1}^{n}(e_i-\mu_0)^2\right) \tag{6}$$

$$P_{(H_1,n)} = \frac{1}{\left(\sigma_1\sqrt{2\pi}\right)^n}exp\left(-\frac{1}{2\sigma_1^2}\sum_{i=1}^{n}(e_i-\mu_1)^2\right) \tag{7}$$

The likelihood ratio is the ratio of the two joint probability densities: The likelihood ratio is the ratio of the two joint probability densities:

$$L_e = \frac{P_{(H_1,n)}}{P_{(H_0,n)}} \tag{8}$$

In the SPRT framework, it is essential to define the Type I error rate α (false alarm rate) and Type II error rate β (miss detection rate). Based on these parameters, the decision thresholds A and B can be calculated as follows:

$$A = \frac{\beta}{1-\alpha} \tag{9}$$

$$B = \frac{1-\beta}{\alpha} \tag{10}$$

The decision rule for the sequential probability ratio is defined as follows. Given an observed residual e_1, the likelihood ratio L_{e_1} is computed. If $L_{e_1} > B$, the alternative hypothesis H_1 is accepted, the test is terminated, and the system is identified as abnormal.

On a system equipped with a 13th-generation Intel i7-13700H CPU and an NVIDIA 4060 GPU, the multi-parameter anomaly detection methods based on MSET and SPRT exhibit low computational complexity throughout the entire process, from memory matrix construction to residual sequence generation. All computations are completed within milliseconds, demonstrating that the methods are capable of meeting real-time

industrial requirements.

3. Methodological framework

The framework of the interpretable adaptive anomaly detection method for multi-condition intelligent equipment monitoring is shown in Figure 1.

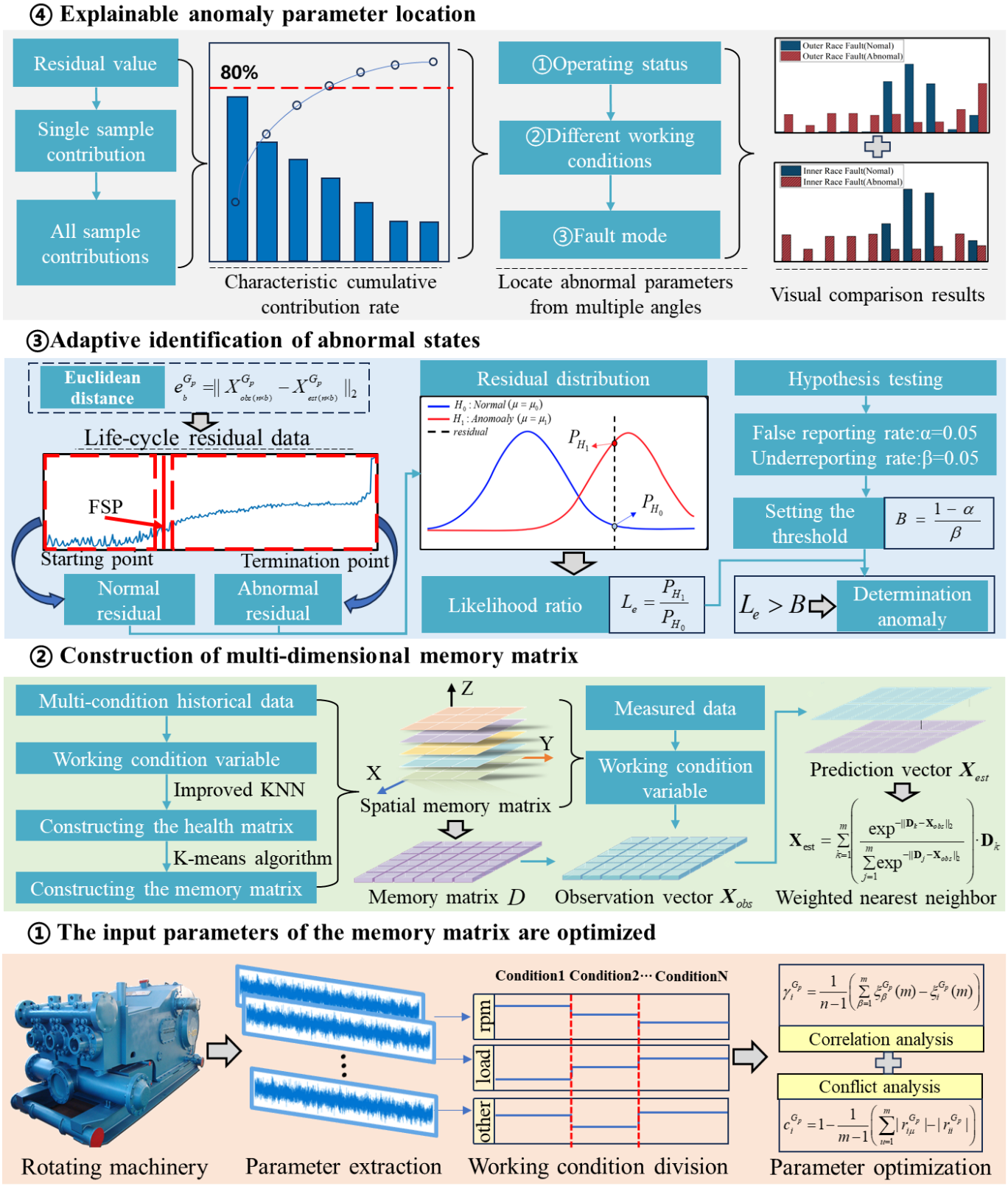

Figure 1. The framework of the interpretable adaptive anomaly detection method for multi-condition intelligent equipment monitoring.

It consists of four key components: optimal selection of input parameters for the MM, construction of the spatial MM, adaptive detection of anomalies, and interpretable localization of abnormal parameters. The procedure is as follows:

1) Sensitivity and correlation analyses are performed using relevance and conflict indices, enhancing parameter sensitivity to changing operating conditions and inter-parameter correlations.
2) A spatial MM is built using an enhanced KNN algorithm and K-means clustering, with a weighted nearest-neighbor method to predict the estimated vectors more accurately.
3) Residuals between the observed and estimated data are quantified using Euclidean distance. These residuals are then evaluated using the weighted nearest-neighbor-based MSET and SPRT to detect anomalies across different conditions.
4) The cumulative contribution rate of features is derived from residuals, with a threshold set to identify dominant abnormal parameters. Multi-parameter contributions are analyzed across operational states, working conditions, and fault modes to enable interpretable analysis and precise anomaly localization.

3.1. Optimal Selection of Input Parameters for the MM

This paper defines the operational state space as G_p, where $G_p \in (G_1, G_2, \ldots\ldots, G_w)$ and w represents the number of operating conditions. On this basis, parameter optimization is achieved from two aspects: the sensitivity of parameters to conditions and the correlation between multi - condition parameters.

1) Analysis of Condition-Sensitive Parameters

Condition - sensitive parameter screening is implemented through grey relational analysis. The core steps are as follows:

(1) Select the $i-th$ monitoring parameter under condition G_p as the reference sequence $x_0^{G_p}(m)$,and the corresponding monitoring data as the comparison sequence $x_i^{G_p}(m)$. The Min - Max normalization method is used to process the sequences. The grey relational coefficient is calculated according to Eq.11, where ρ is the resolution coefficient, commonly set to 0.5.

$$\xi_i^{G_p}(m) = \frac{\min\limits_i \min\limits_m \left|x_0^{G_p}(m) - x_i^{G_p}(m)\right| + \rho \cdot \max\limits_i \max\limits_m \left|x_0^{G_p}(m) - x_i^{G_p}(m)\right|}{\left|x_0^{G_p}(m) - x_i^{G_p}(m)\right| + \rho \cdot \max\limits_i \max\limits_m \left|x_0^{G_p}(m) - x_i^{G_p}(m)\right|} \tag{11}$$

(2) Based on the grey relational coefficient, the correlation $\gamma_i^{G_p}$ between the $i-th$ feature parameter and the other feature parameters is calculated. The mean value is then used for centralization to reflect the correlation between each monitoring parameter and the reference sequence, as shown in Eq.12:

$$\gamma_i^{G_p} = \frac{1}{n-1}\left(\sum_{\beta=1}^{m} \xi_\beta^{G_p}(m) - \xi_i^{G_p}(m)\right) \tag{12}$$

(3) Compare the relational degrees of parameters under different conditions G_p and $G_p^{'}$ are compared, and calculate the parameter sensitivity index S_i as shown in Eq.13:

$$S_i = \frac{\gamma_i^{G_p^{'}}}{\gamma_i^{G_p}} \tag{13}$$

When a parameter can well track the condition changes of rotating equipment, there will be an obvious difference between $\gamma_i^{G_p}$ and $\gamma_i^{G_p^{'}}$, and the parameter condition sensitivity S_i will deviate from one.

2) Multi-condition Correlation Analysis

To quantify this inter-parameter conflict under varying conditions, a correlation analysis approach is introduced. Assume that the feature parameter sequence under operating conditions G_p is defined as $\boldsymbol{X}^{G_p}$.

$$\boldsymbol{X}^{G_p} = [\boldsymbol{x}_1 \quad \boldsymbol{x}_2 \quad \cdots \quad \boldsymbol{x}_n]^T = \left[x_{ij}\right]_{n\times m} \tag{14}$$

where $\boldsymbol{x}_i$ denotes the feature data sequence of the $i-th$ feature parameter, and x_{ij} represents the feature data of the $i-th$ feature parameter collected at the $j-th$ sampling point.

The correlation coefficient between parameter i and parameter μ is then computed based on this matrix:

$$r_{i\mu}^{G_p} = \frac{\sum_{j=1}^{m}\left(x_{ij} - \bar{x}_i\right)\left(x_{\mu j} - \bar{x}_\mu\right)}{\sqrt{\sum_{j=1}^{m}\left(x_{ij} - \bar{x}_i\right)^2 \sum_{j=1}^{m}\left(x_{\mu j} - \bar{x}_\mu\right)^2}} \tag{15}$$

where $\mu = 1,2,\cdots,n$. The conflict index between feature parameter i and the remaining feature parameters μ under operating condition G_p is given by Equation (16):

$$c_i^{G_p} = 1 - \frac{1}{m-1}\left(\sum_{u=1}^{m} |r_{i\mu}^{G_p}| - |r_{ii}^{G_p}|\right) \tag{16}$$

At this point, a smaller value of $c_i^{G_p}$ indicates lower conflict among the parameters, stronger inter-parameter connections, and a closer association with the equipment status.

3.2. Construction of the Spatial MM

Considering the wide range of operating condition variations in rotating equipment and the strong fluctuation of monitoring parameters during operation, directly using all the available

process data to construct a MM may lead to poor modeling performance. To address this, this study proposes a working-condition-oriented selection strategy for monitoring the parameters. By incorporating an improved KNN algorithm and k-means clustering, a spatial MM under multiple conditions is constructed to enhance the accuracy and adaptability of the model.

Given complex environmental noise affecting on-site signals, abnormal data samples must be removed. The top 95% healthy samples are selected based on KNN, and combined with K-means clustering centers to construct the MM. The procedure is as follows:

Step 1: Input the historical dataset under normal operating conditions, denoted as $L_{n\times l} = [\boldsymbol{X}(t_1)\boldsymbol{X}(t_2)\cdots\boldsymbol{X}(t_l)]$, where $l \geq m$. Based on the operating condition parameters, the dataset is assigned to its corresponding working condition space G_p.

Step 2: Calculate the average value of each monitoring parameter $v_{L,1}$ under the operating condition space, and obtain the mean vector: $\boldsymbol{V}_L^{G_p} = \left[v_{L,1}, v_{L,2}, \cdots, v_{L,n}\right]^T$.

Step 3: Calculate the Euclidean distance d_j between each state vector in $L_{n\times l}$ and the mean vector $\boldsymbol{V}_L^{G_p}$ to obtain the distance vector: $\boldsymbol{R}_{ist}^{G_p} = [d_1, d_2, \cdots, d_l]^T$. Distance d_j is computed using the Euclidean formula:

$$d_j\left(\boldsymbol{X}(t_j), \boldsymbol{V}_L^{G_p}\right) = ||\boldsymbol{X}(t_j) - \boldsymbol{V}_L^{G_p}||_2 = \sqrt{\sum_{i=1}^{n}\left(x_i(t_j) - v_{L,i}\right)^2} \quad (17)$$

Step 4: Sort the elements of the distance vector $\boldsymbol{R}_{ist}^{G_p}$ in ascending order and select the first 95% of the samples with the smallest distances as healthy samples. Let the number of selected samples be ρ_1, where $\rho_1 = 95\% \times l$. The state vectors corresponding to these ρ_1 elements are extracted to construct the health matrix $\boldsymbol{H}_{n\times\rho 1}^{G_p}$.

Step 5: Randomly select ρ_2 state vectors from ρ_1 samples to serve as initial cluster centers: $\boldsymbol{C} = [c_1, c_2, \cdots, c_{\rho 2}]$.

Step 6: Compute the Euclidean distance between each state vector and the cluster centers using $\boldsymbol{C}$.

Step 7: Assign each sample to its nearest cluster center and update the cluster centers based on the new grouping results.

Step 8: Repeat Steps 6 and 7 until the cluster centers no longer change.

Step 9: The final ρ_2 cluster centers are used as representative state vectors to construct the initial MM, $\boldsymbol{D}_{n\times\rho_2}^{G_p}$. To address the varying operating condition regions determined by the condition identification parameter, q healthy historical samples under each operating condition serve as training data: $\{\boldsymbol{L}_{n\times q}^{G_1}, \boldsymbol{L}_{n\times q}^{G_2}\ldots\boldsymbol{L}_{n\times q}^{G_w}\}$, where $q \geq m$. Repeat Steps 1-9 to construct a MM set under multiple working conditions: $\{\boldsymbol{D}_{n\times\rho_2}^{G_1}, \boldsymbol{D}_{n\times\rho_2}^{G_2}\ldots\boldsymbol{D}_{n\times\rho_2}^{G_w}\}$. Given b real-time observation data samples under different operating conditions, $\{\boldsymbol{X}_{obs(n\times b)}^{G_1}, \boldsymbol{X}_{obs(n\times b)}^{G_2}\cdots\boldsymbol{X}_{obs(n\times b)}^{G_w}\}$, the corresponding MM is determined based on the condition identification parameter, and the estimation vector set $\{\boldsymbol{X}_{est(n\times b)}^{G_1}, \boldsymbol{X}_{est(n\times b)}^{G_2}\cdots\boldsymbol{X}_{est(n\times b)}^{G_w}\}$ is obtained according to Eq. (4).

3.3. Adaptive Identification of Abnormal Conditions

The residual sequence between the estimated and observed vectors under multiple operating conditions is calculated based on Euclidean distance, as shown in Eq. (18). Let the residual vectors be $\boldsymbol{e}_b^{G_p}, \boldsymbol{e}_b^{G_p} \in \{\boldsymbol{e}_b^{G_1}, \boldsymbol{e}_b^{G_2}\ldots\boldsymbol{e}_b^{G_w}\}$.

$$\boldsymbol{e}_b^{G_p} = ||\boldsymbol{X}_{obs(n\times b)}^{G_p} - \boldsymbol{X}_{est(n\times b)}^{G_p}||_2 \quad (18)$$

The SPRT is used to perform a tracking analysis of the residual sequence to determine whether an abnormal signal is present. Under G_p, the mean $\mu_0^{G_p}$ and standard deviation $\sigma_0^{G_p}$ of the residuals are calculated from normal operating data. In practical applications, the occurrence of faults often leads to changes in the residual mean, such that it increases or decreases. Therefore, the mean under the abnormal condition is defined as $\mu_1^{G_p} = \mu_0^{G_p} + \Delta\mu$, where $\Delta\mu$ is set to $3\sigma_0^{G_p}$. The variances under normal and abnormal conditions are considered equal, that is, $(\sigma_1^{G_p})^2 = (\sigma_0^{G_p})^2$. In the SPRT, both the false alarm rate and the miss detection rate are set to 0.05. By leveraging Equations (6)-(10) and integrating the sequential probability ratio criterion, an adaptive response to the evolution process of abnormal states under multi - operating conditions of rotating equipment is achieved.

3.4. Interpretable Localization of Abnormal Parameters

The combined MSET and SPRT approach allows real-time discrimination of the operating state of rotating equipment but lacks precise traceability of anomaly parameters. To overcome this, a cumulative contribution analysis framework based on error statistics is proposed. This framework sequentially calculates errors, evaluates cumulative contribution rates, models parameter contribution trajectories, and selects key parameters, enabling interpretable localization of anomalies.

Based on the analytical framework, the squared prediction error of the $i-th$ parameter at time j is defined as:

$$E(i,j) = (X_{\text{obs}}(i,j) - X_{\text{est}}(i,j))^2 \quad (19)$$

$X_{\text{obs}}(i,j)$ and $X_{\text{est}}(i,j)$ denote the observed and estimated values, respectively.

To balance the relative impact of each parameter's error over the entire monitoring duration, the instantaneous contribution rate is introduced and defined as:

$$E_r(i,j) = \frac{E(i,j)}{\sum_{i=1}^{n} E(i,j)} \quad (20)$$

Here, $E_r(i,j)$ reflects the contribution of the $i-th$ parameter to the total error at time j, enabling comparison across different monitored parameters.

By aggregating the contribution rates over time, a two-dimensional matrix $\boldsymbol{E}_r$ can be constructed:

$$\boldsymbol{E}_r = \begin{bmatrix} E_r(1,1) & E_r(1,2) & \cdots & E_r(1,m) \\ E_r(2,1) & E_r(2,2) & \cdots & E_r(2,m) \\ \vdots & \vdots & \ddots & \vdots \\ E_r(n,1) & E_r(n,2) & \cdots & E_r(n,m) \end{bmatrix} \quad (21)$$

The matrix $\boldsymbol{E}_r$ records the contribution trajectories of each monitored parameter across the monitoring period, serving as the basis for interpretable parameter anomaly diagnosis.

On this basis, the cumulative contribution rate $E_{cr}(i)$ is introduced to quantify the overall abnormality level of each parameter throughout the monitoring period:

$$E_{cr}(i) = \frac{1}{m}\sum_{j=1}^{m} E_r(i,j) \quad (22)$$

A higher value of $E_{cr}(i)$ indicates a greater contribution of the corresponding parameter to the overall anomaly, which facilitates the identification of key abnormal parameters.

Based on $E_{cr}(i)$,construct the index set of main abnormal monitoring parameters:

$$A = \left\{ i | E_{cr}(i) = \max_{i'} E_{cr}(i') \right\} \quad (23)$$

Considering the background of the multi - parameter abnormal detection model constructed in this paper, set the threshold δ of the cumulative abnormal contribution rate of multi - parameters, and screen out the multi - parameter set that exceeds the threshold.

$$A_\delta = \{ i | E_{cr}(i) \geq \delta \} \quad (24)$$

4. Experiments and Results

4.1. Experimental setup

4.1.1. Experimental Dataset Introduction

To validate the effectiveness of the proposed method, experiments are conducted using the publicly available XJTU-SY full life-cycle bearing dataset provided by the Xi'an JiaoTong University [26]. The experimental setup is illustrated in Figure 2. The sampling frequency is 25.6 kHz, with each sampling lasting 1.28 seconds and performing at 1-minute intervals. Horizontal vibration data under three different operating conditions are selected for analysis. The detailed information is provided in Table 1.

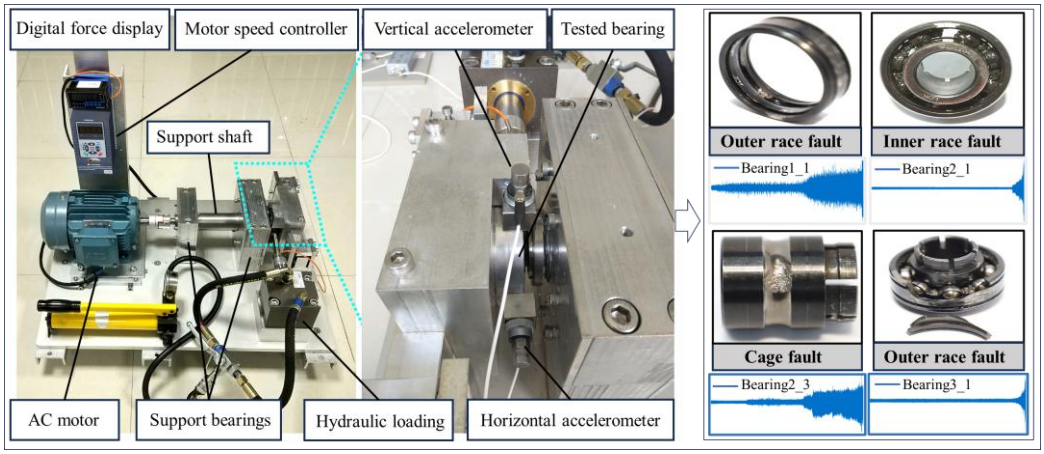

Figure 2. Experimental test bench.

Table 1. Rolling bearing dataset.

Case number	Operating condition	Dataset	Number of files	Bearing lifetime	Fault element
1	Speed: 2100 r/min Load: 12 kN	Bearing1_1	123	2h3min	Outer ring
2	Speed: 2250 r/min Load: 11 kN	Bearing2_1	491	8h11min	Inner ring
		Bearing2_3	533	8h53min	Cage
3	Speed: 2400 r/min Load: 10 kN	Bearing3_1	2538	42h18min	Outer ring

To extract informative features from one-dimensional raw signals collected under different operating conditions, multi-domain feature extraction is performed, and the detailed features are summarized in Table 2.

Specifically, the correlation of feature parameters was calculated separately for the Bearing1_1–Bearing3_1 dataset and the Bearing2_1–Bearing3_1 dataset, yielding two sets of average sensitivity indices under different operating conditions, as shown in Figure 3. Based on Figure 3, the average sensitivity index of each feature was compared with the absolute deviation from 1 to quantify the sensitivity of each feature to operating condition variations. A threshold of 0.2 was determined using the 75th percentile. Considering that the deviation values of features $t11$ and $t18$ were 0.199, only 0.001 below the threshold, and that the overall standard deviation was 0.707, $t11$ and $t18$ were retained in the selected feature set. Consequently, the final set of features included $t5$, $t6$, $t7$, $t10$, $t11$, $t18$, $t19$, $t20$, $t23$, $t24$, and $t25$.

After feature selection based on sensitivity indices, conflict indices were further calculated to assess the inter-feature relationships. Data from three different operating conditions—Bearing1_1, Bearing2_1, and Bearing3_1—were used to compute the conflict indices, as shown in Figure 4. Using a two-standard-deviation criterion to set the threshold, statistical analysis revealed that only feature $t25$ exceeded the threshold across all three operating conditions. The abnormally high conflict index of $t25$ also indicated weak correlation with other features.

Ultimately, the final feature set for condition monitoring is established as $T = [t5, t6, t7, t10, t11, t18, t19, t20, t23, t24]$.

Table 2. Multi-domain feature collection and label information.

Time-Domain Features ($t1 - t17$)	$t1 - t3$: Maximum, minimum, and mean values $t4 - t6$: Peak value, absolute mean, and variance $t7 - t9$: Standard deviation, skewness, and kurtosis $t10 - t12$: Root mean square (RMS), root amplitude, and peak value $t13 - t17$: Crest factor, clearance factor, impulse factor, shape factor, and vibration intensity
Frequency-Domain Features ($t18 - t23$)	$t18 - t20$: Center frequency, mean square frequency, and RMS frequency $t21 - t23$:Frequency variance, frequency standard deviation, and mean frequency amplitude
Time–Frequency Domain Features ($t24 - t31$)	$t24 - t31$: Energy ratios of 8 frequency bands obtained via three-level wavelet packet decomposition

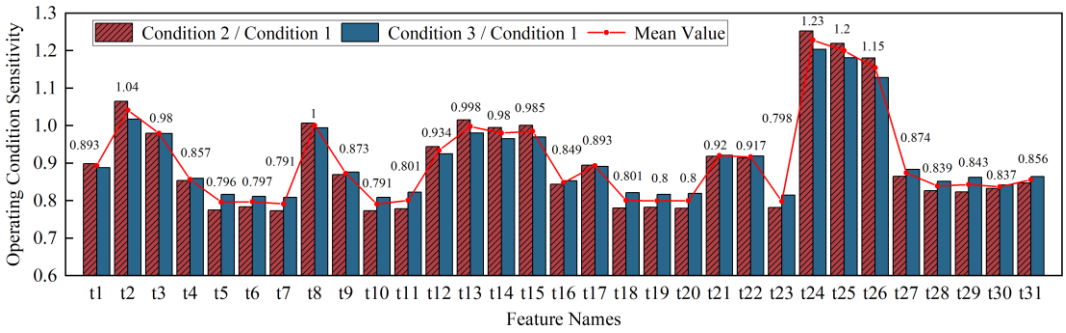

Figure 3. Condition sensitivity indicator result graph.

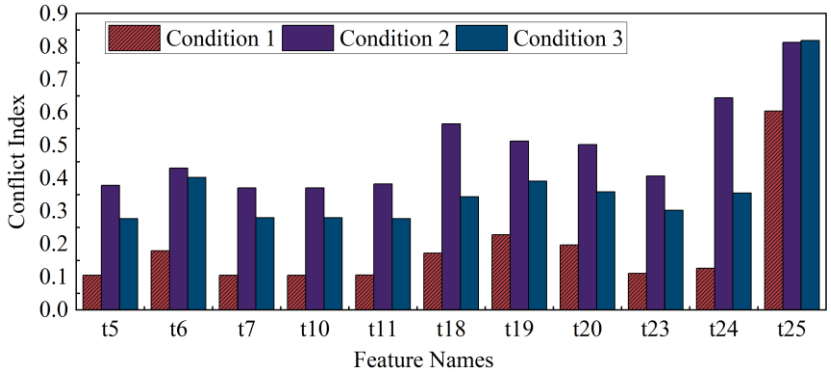

Figure 4. Conflict indicator result graph.

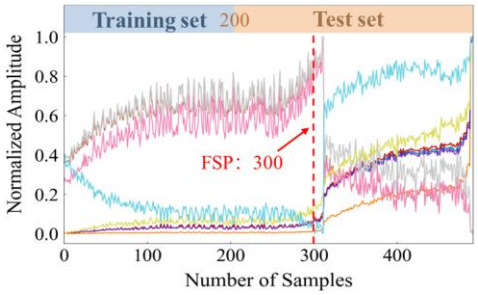

(a) Feature Trajectories of Bearing1_1

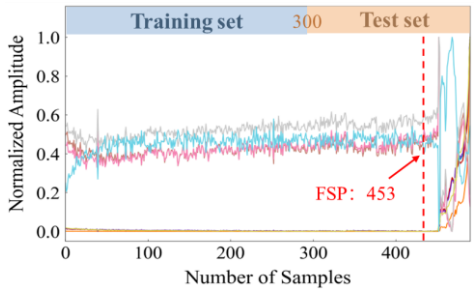

(b) Feature Trajectories of Bearing2_1

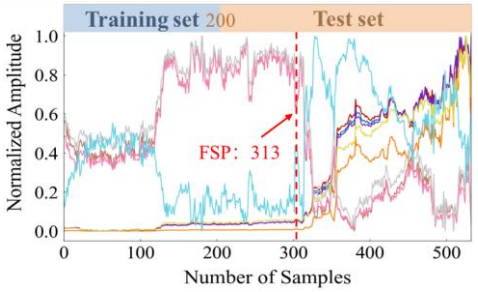

(c) Feature Trajectories of Bearing2_3

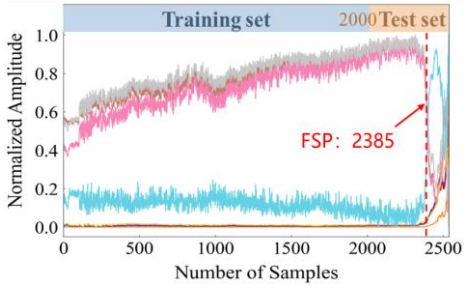

(d) Feature Trajectories of Bearing3_1

Figure 5. Feature curves of the multi-condition bearing dataset.

4.1.2. Data Partitioning

Rotating machinery typically operates in healthy conditions for the majority of its bearing life cycle. After the onset of an unidentified anomaly, minor fault characteristics gradually emerge. The time at which these initial fault symptoms appear is defined as the Failure Start Point (FSP), The FSP in the full life cycle data is determined using the three-sigma (3σ) method [10]. Considering the relatively limited number of samples in the Bearing1_1 dataset, the data is segmented into four groups using a sliding window approach. The specific locations of the failure start points and the data segmentation scheme under different working conditions are illustrated in Figure 5.

To validate the rationality of the selected healthy data, analyses were conducted using different retention ratios of the healthy dataset, as illustrated in the Figure 6. Four sets of training data were employed as historical normal-state datasets. The results indicate that retaining the top 95% of the data with the smallest healthy distances can effectively suppress the influence of outliers while achieving minimal and stable healthy distance values, thereby further enhancing the accuracy and reliability of the data. This approach is particularly suitable for industrial applications.

In the analysis of multi-operating-condition datasets, to mitigate the instability caused by differences in sample sizes across conditions, the clustering parameter was set to ρ_2=100. This setting maintains a relatively consistent clustering resolution across datasets of varying scales, thereby reducing the potential impact of sample size differences on clustering performance. Simultaneously, it decreases the scale of the memory matrix and redundant computations, improving the overall computational efficiency of the model.

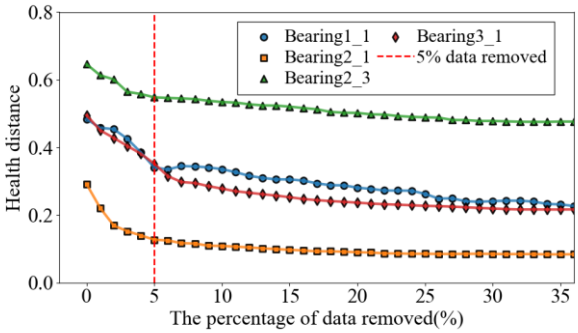

Figure 6. Different percentage effect diagrams.

4.2. Result analysis

4.2.1. Performance Analysis of the Model

To evaluate the overall performance of the proposed MSET-SPRT method in multi-parameter anomaly detection tasks, a comparative study is conducted against four baseline methods: OC-SVM, IF, PCA, Autoencoder(AE), Transformer ,Graph Neural Network (GNN).

Performance was evaluated using classification metrics, including accuracy, recall, precision, F1-score, and AUC [27]. Each model was evaluated ten times, and the mean values of the

metrics were used to conduct statistical significance testing to compare model performance. The comparison of classification performance between the proposed method and baseline methods is summarized in Table 3.

Table 3. Comparison of classification accuracy indicators.

Methods	Operating conditions	accuracy	precision	recall	F1-score	AUC
OC-SVM	Condition 1 (Bearing1_1)	0.9486	0.9279	1.0000	0.9626	0.9242
IF		0.9726	0.9602	1.0000	0.9797	0.9596
PCA		0.9384	0.9147	1.0000	0.9554	0.9091
AE		0.9623	0.9789	0.9637	0.9713	0.9617
Transformer		0.9795	0.9845	0.9845	0.9845	0.9771
GNN		0.9760	0.9844	0.9793	0.9818	0.9745
MSET-SPRT		0.9829	0.9845	0.9896	0.9871	0.9797
OC-SVM	Condition 2 (Bearing2_1)	0.9738	0.8864	1.0000	0.9398	0.9836
IF		0.9424	0.7800	1.0000	0.8764	0.9638
PCA		0.9058	0.6842	1.0000	0.8125	0.9408
AE		0.9529	0.9688	0.7949	0.8732	0.8941
Transformer		0.9634	0.9000	0.9231	0.9114	0.9484
GNN		0.9791	0.9730	0.9231	0.9474	0.9582
MSET-SPRT		0.9843	0.9286	1.0000	0.9630	0.9901
OC-SVM	Condition 2 (Bearing2_3)	0.9339	0.9095	1.0000	0.9526	0.9018
IF		0.8438	0.8095	1.0000	0.8947	0.7679
PCA		0.8679	0.8340	1.0000	0.9095	0.8036
AE		0.9309	0.9853	0.9095	0.9459	0.9414
Transformer		0.9369	1.0000	0.9050	0.9501	0.9525
GNN		0.9429	0.9951	0.9186	0.9553	0.9548
MSET-SPRT		0.9520	1.0000	0.9276	0.9624	0.9638
OC-SVM	Condition 3 (Bearing3_1)	0.9164	0.7739	1.0000	0.8725	0.9414
IF		0.8959	0.7333	1.0000	0.8462	0.9271
PCA		0.8922	0.7264	1.0000	0.8415	0.9245
AE		0.9461	0.9845	0.8247	0.8975	0.9097
Transformer		0.9703	1.0000	0.8961	0.9452	0.9481
GNN		0.9647	1.0000	0.8766	0.9343	0.9383
MSET-SPRT		0.9796	1.0000	0.9286	0.9630	0.9643

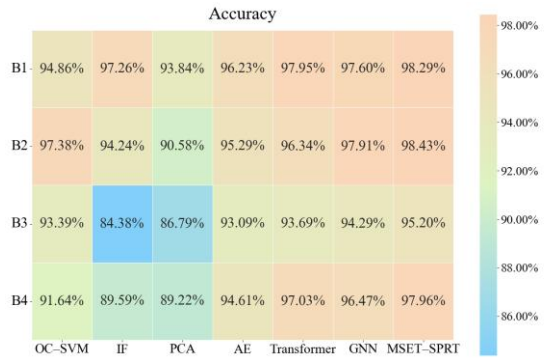

(a) Comparison of Accuracy

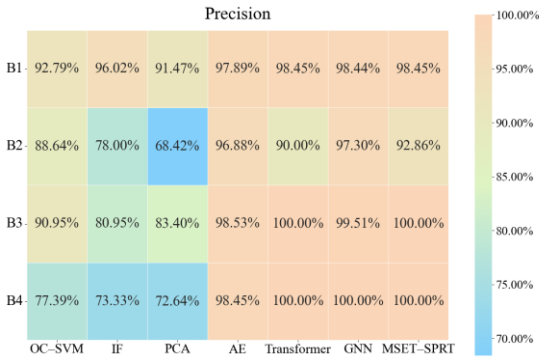

(b) Comparison of Precision

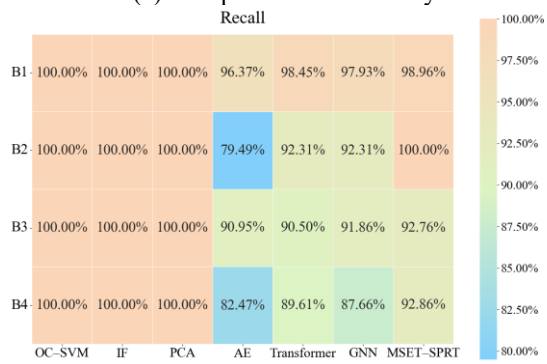

(c) Comparison of Recall

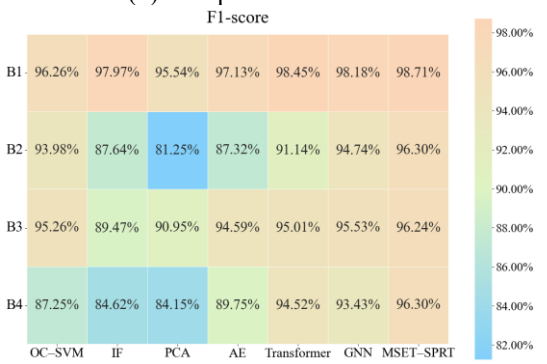

(d) Comparison of F1-Score

Figure 7. Heat maps of data classification indicators for different working conditions.

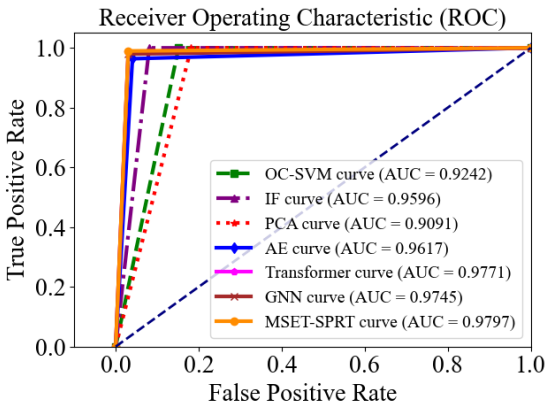

(a) ROC Curve of Bearing1_1

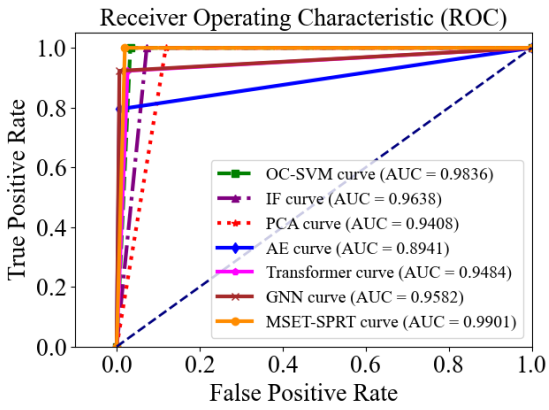

(b) ROC Curve of Bearing2_1

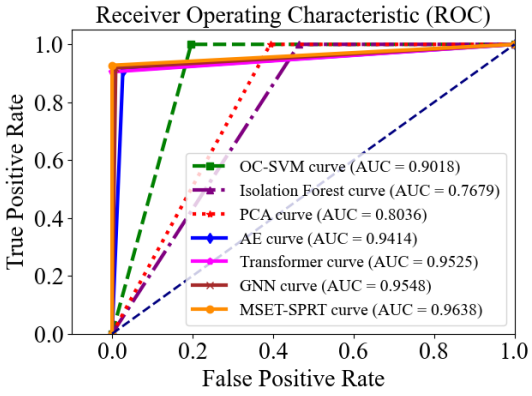

(c) ROC Curve of Bearing2_3

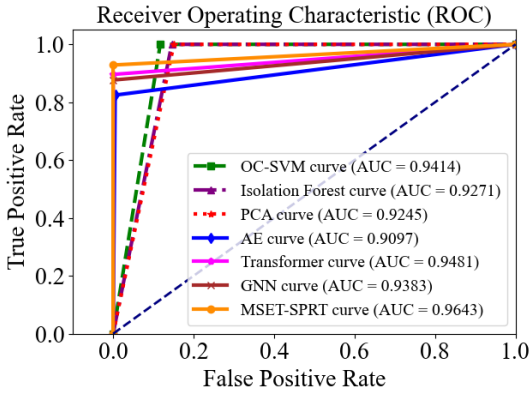

(d) ROC Curve of Bearing3_1

Figure 8. ROC curve comparison chart of datasets with different working conditions.

The proposed MSET-SPRT multi-parameter anomaly detection method demonstrates superior overall performance across different bearing datasets under varying operating conditions. It achieved an average classification accuracy of 97.47%, and consistently yielded the highest AUC scores among all compared methods. These results indicate the strong generalization capability and robustness of the proposed method in diverse operational scenarios.

For clarity, the four bearing datasets used in this study are labeled B1-B4, corresponding to different working conditions. The detailed classification metrics in the form of a heatmap and receiver operating characteristic (ROC) curves are illustrated in Figure 7 and Figure 8, respectively.

4.2.2. Interpretability Analysis

This paper provides an interpretable localization of anomaly parameters by quantifying the residual contributions. The Cumulative Abnormal Contribution Rate (CACR) for all abnormal residual samples is first calculated according to Eq. 22. Figure 9 shows the CACR ranking curves for each feature in four sets of bearing data, with the right y-axis indicating the multi-parameter CACR. Based on Eq. 24, a threshold reference line is set when the multi-parameter CACR reaches 80%[28], ensuring the completeness of the dominant anomaly variables while eliminating redundant features. When the multi-parameter CACR exceeds the threshold, the corresponding feature subset represents the dominant anomaly feature set in the dataset. The dominant anomaly feature sets, $A_{\delta 1-1} = \{t24, t23, t7, t10, t18, t5, t11\}$, $A_{\delta 2-1} = \{t23, t11, t5, t7, t10, t24, t20\}$, $A_{\delta 2-3} = \{t7, t10, t5, t11, t23, t6, t24\}$ and $A_{\delta 3-1} = \{t24, t18, t19, t20, t23, t11\}$ are shown in Figure 9(a), (b), (c), and (d), respectively. From these dominant anomaly feature sets, key characteristics affecting the anomalies can be identified, which primarily include time-domain and frequency-domain impact features as well as low-frequency energy features.

To further explore the interpretability of dominant features in anomaly localization, this paper analyzes the trend differences of the cumulative contribution rates of features from multiple perspectives, including operating states, working conditions, and fault types.

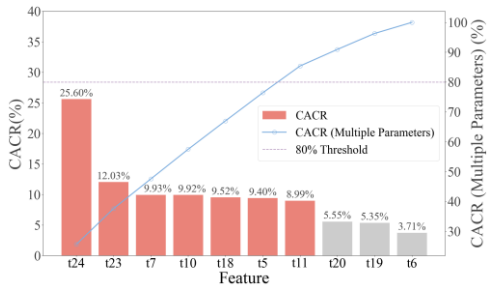

(a) CACR ranking of features in dataset Bearing1_1

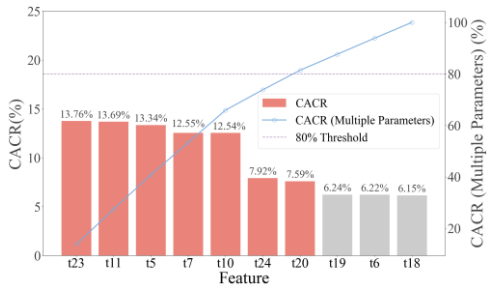

(b) CACR ranking of features in dataset Bearing2_1

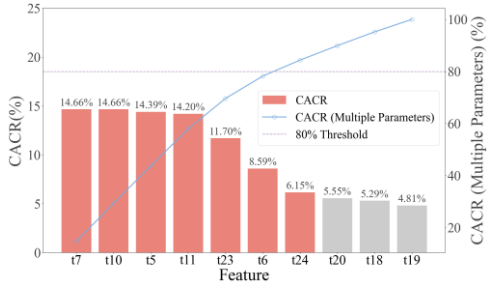

(c) CACR ranking of features in dataset Bearing2_3

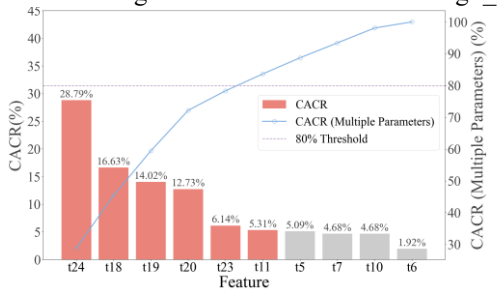

(d) CACR ranking of features in dataset Bearing3_1

Figure 9. Ranking curves of feature CACR under different operating conditions.

A comparative chart illustrating the cumulative contribution rates under different conditions is presented in Figure10. It is evident that there are significant differences in the contribution trends under normal and faulty conditions. In the normal state, residuals are generally small, and the dominant contributing features include $t18$, $t19$, $t20$, and $t24$. These features reflect the characteristics of healthy bearings, where the vibration signals exhibit low energy and stability, with spectral energy concentrated in the low-frequency band and absence of distinct fault frequencies. Features $t18$, $t19$, $t20$ indicates the spectral energy concentration, whereas $t24$ directly quantifies the proportion of low-frequency energy.As the bearing condition transitions from normal to faulty, the signal energy distribution undergoes a significant reconstruction. The energy shifts from the dominant low-frequency band to fault-related frequencies and high-frequency resonance regions, leading to a decrease in spectral energy concentration. This redistribution reduces the cumulative contributions of $t18$, $t19$, $t20$, and $t24$ under fault conditions. However, for the outer-race faults, an exception is observed, as shown in Figure 10(a) and Figure 10(d). Despite the overall dispersion in spectral energy, the contribution rate of feature $t24$ increases under fault conditions. This behavior is attributed to the structural configuration of the outer race, which is rigidly connected to the bearing housing. Fault-induced impact energy is transmitted directly through this rigid path, resulting in minimal attenuation of low-frequency components. Consequently, the base frequency and nearby harmonics of the impact energy are better preserved, leading to a relative increase in the low-frequency energy concentration. This phenomenon highlights $t24$ as a key indicator of outer-race faults, especially under conditions where the low-frequency shock energy stands out against the background of overall spectral dispersion.

A comparative analysis of Bearing1_1 (high load, low speed) and Bearing3_1 (low load, high speed) under outer race fault conditions, as shown in Figure 10(a) and Figure 10(d), reveals the significant influence of operating conditions on multi-domain feature contributions. Under abnormal conditions, a high load and low speed lead to an increase in the cumulative contribution of time-domain statistical features and average frequency-domain amplitude features. A high load enhances contact stress and friction, resulting in an increased signal amplitude in the time domain. Meanwhile, the lower rotational speed allows for longer energy accumulation between impacts, amplifying individual shock events and enhancing time-domain indicators and global energy-related frequency features. In contrast, under low load and high speed, the high-frequency excitation of rotating components more easily resonates with the fault characteristic frequencies, causing energy to concentrate near these frequencies and their harmonics. This condition increases the contribution of the spectral features of $t18 - t20$ and $t24$. Thus, the interaction between the load and speed significantly affects the intensity of the fault excitation, energy distribution pattern, and its representation across different domains. Specifically, a high load enhances the

amplitude-based and time-domain features, whereas a high speed is more favorable for emphasizing the frequency-domain energy concentration. These insights underscore the necessity of tailoring feature extraction and diagnostic strategies to specific operating conditions: frequency-domain energy distribution features should be emphasized under low-load, high-speed conditions, whereas time-domain statistical indicators and amplitude features are more informative under high-load, low-speed scenarios.

Figure 10(b) and Figure 10(c) present the cumulative feature contributions for inner race faults (Bearing2_1) and cage faults (Bearing2_3) under identical operating conditions. In the normal state, inner race faults tend to exhibit higher contributions from $t20$ owing to distributed low-frequency impacts and modulation components, whereas $t18$ is relatively low. Conversely, cage faults exhibit a strong energy concentration around intrinsic low-frequency modes and their harmonics, producing the opposite trend. However, under fault conditions, the vibrational coupling between physically adjacent components leads to convergence in feature contribution trends, thereby reducing the discriminability between fault types.

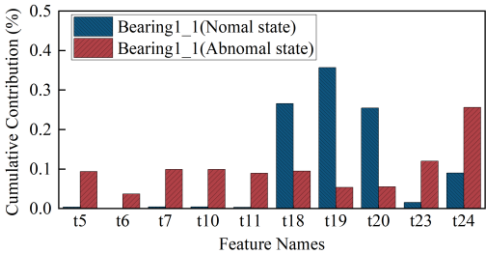

(a) Cumulative Feature Contribution Rate of Bearing1_1

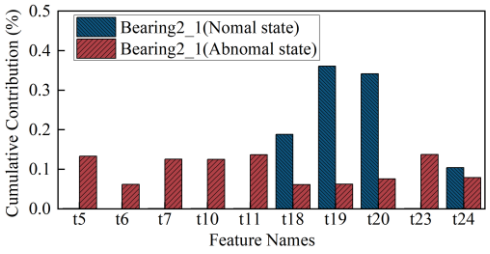

(b) Cumulative Feature Contribution Rate of Bearing2_1

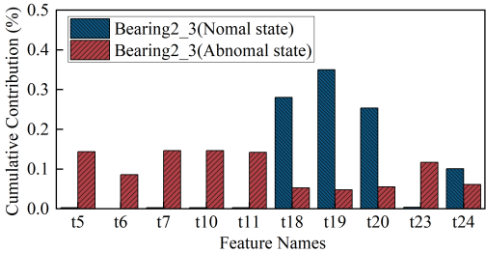

(c) Cumulative Feature Contribution Rate of Bearing2_3

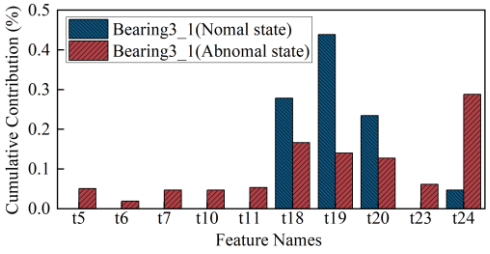

(d) Cumulative Feature Contribution Rate of Bearing3_1

Figure 10. Comparison of feature cumulative contribution rates under different operating states.

5. Discussion

5.1. Generalization Ability Assessment on Multiple Datasets

To further validate the generalization capability of the proposed model, three full-life bearing datasets under different operating conditions from the IEEE PHM 2012 dataset were selected for analysis, including the Learning sets Bearing1_1, Bearing2_1, and Bearing3_1 [29]. Based on sensitivity and conflict analyses, the feature subset $T_P = [t1, t4, t5, t7, t10, t11, t12, t18, t22, t23]$ was determined for model construction and metric evaluation. Considering the limited space of this paper, only the results for Bearing1_1 are presented, as shown in the table 4. The MSET-SPRT method demonstrates significant advantages across different datasets in terms of comprehensive performance metrics.

Table 4. Comparison of Evaluation Metrics for the PHM Bearing1_1 Dataset.

Methods	Operating conditions	accuracy	precision	recall	F1-score	AUC
OC-SVM	Condition1 (Bearing1_1)	0.8895	0.8362	0.9959	0.9091	0.8764
IF		0.8258	0.7616	0.9986	0.8642	0.8045
PCA		0.8388	0.8734	0.8299	0.8511	0.8399
AE		0.9041	0.9530	0.8700	0.9096	0.9083
Transformer		0.9447	0.9670	0.9322	0.9493	0.9463
GNN		0.9110	0.9496	0.8866	0.9170	0.9140
MSET-SPRT		0.9509	0.9596	0.9516	0.9556	0.9508

5.2. Performance Comparison of Memory Matrices

To verify the estimation accuracy of the proposed MM construction method (M4), three alternative approaches are compared. M1: Gaussian Mixture Model (GMM)-based clustering; M2: Uniform sampling method; and M3: K-means clustering method.

To quantitatively compare the accuracy of these methods, the Bearing1_1, Bearing2_1, and Bearing3_1 multi-condition bearing datasets are employed. The root-mean-square error (RMSE) [30] and Mean Absolute Percentage Error (MAPE) [31] are computed separately for normal and faulty operating conditions. The results, summarized in Table 5, indicate that the proposed method achieves the lowest error metrics during normal operation, while exhibiting the highest overall performance metrics during faulty states. This significant variation in performance indicators enables effective discrimination between the operating states, thereby providing a reliable basis for anomaly detection.

Table 5. Performance index comparison.

Methods	Bearing1_1 (Normal)		Bearing1_1 (Abnormal)		Bearing2_1 (Normal)		Bearing2_1 (Abnormal)		Bearing3_1 (Normal)		Bearing3_1 (Abnormal)	
	σ_{RMSE}	σ_{MAPE}	σ_{RMSE}	σ_{MAPE}	σ_{RMSE}	σ_{MAPE}	σ_{RMSE}	σ_{MAPE}	σ_{RMSE}	σ_{MAPE}	σ_{RMSE}	σ_{MAPE}
M1	0.0642	29.29%	0.3279	111.13%	0.0307	215.05%	0.2827	183.38%	0.1145	36.33%	0.2745	93.28%
M2	0.0651	30.97%	0.3244	110.67%	0.0392	324.02%	0.2808	178.04%	0.1097	34.95%	0.2749	92.08%
M3	0.0542	25.35%	0.3317	112.55%	0.0293	184.74%	0.2814	182.31%	0.0949	33.55%	0.2888	98.04%
M4	0.0513	24.10%	0.3358	113.71%	0.0287	159.93%	0.2840	183.42%	0.0865	32.93%	0.2959	100.29%

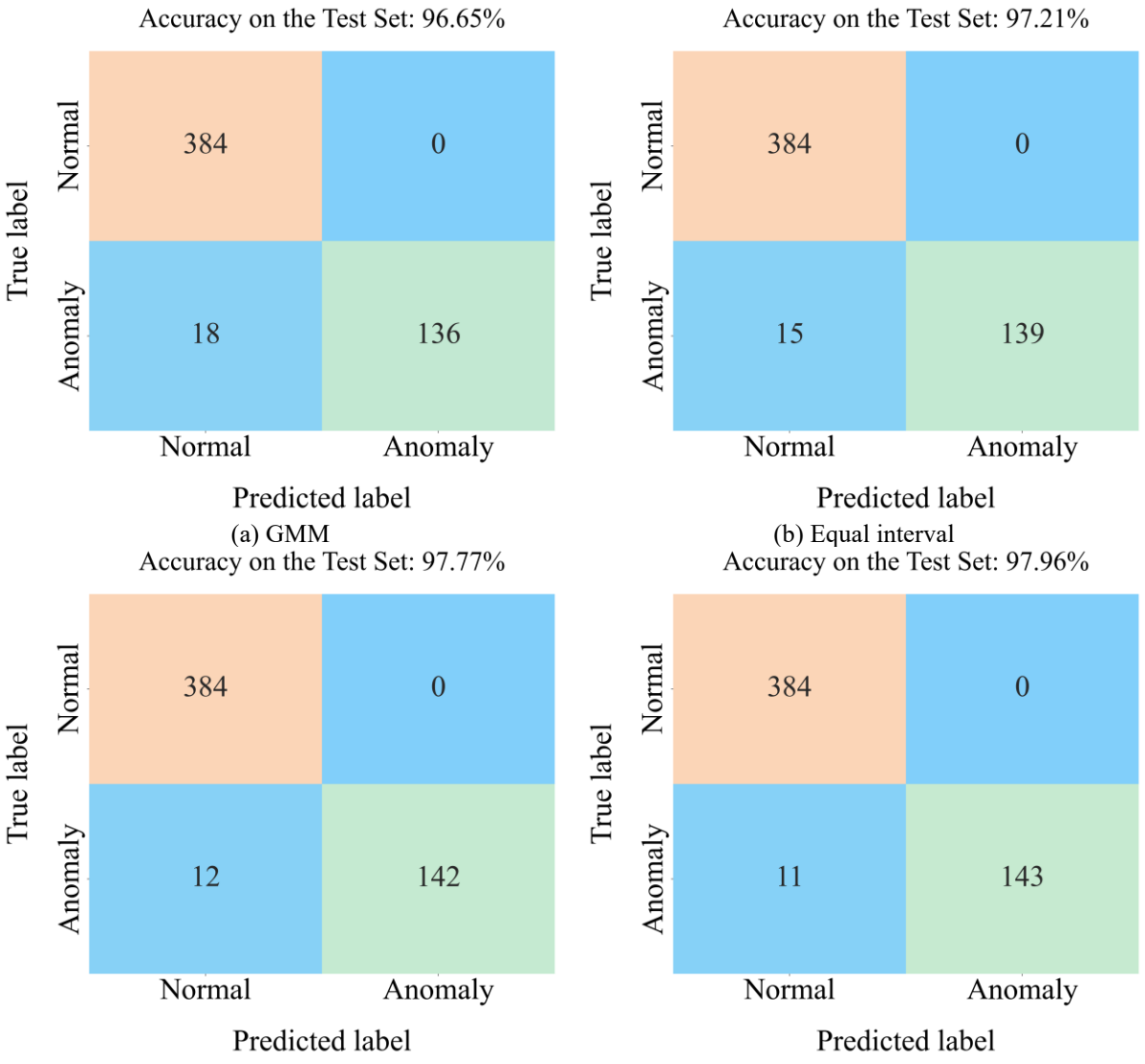

(a) GMM (b) Equal interval

(c) K-means (d) Proposed method

Figure 11. Comparison of accuracy of anomaly detection models based on different MM constructions.

To further investigate the impact of different MM construction methods on the anomaly detection model, this study combines the four aforementioned memory matrices with the SPRT method to evaluate their influence on the performance of the subsequent anomaly detection models. The results are presented in Figure 11. Considering the large volume of real operational data from rotating machinery, the Bearing3_1 dataset is selected as the test benchmark. The confusion matrix results are shown in the figure below. The anomaly detection model constructed by combining the proposed MM method with the SPRT achieved an accuracy of 97.96% on the test set, outperforming the alternative methods in terms of classification accuracy.

5.3. Comparison of Interpretability Analyses

This paper introduces KernelSHAP, a model-agnostic variant of SHAP, to construct an MSET-SHAP interpretability prediction model based on the full-cycle residuals. The results are compared with those from the cumulative contribution rate interpretability analysis, exploring the precision of anomaly parameter localization from multiple perspectives.

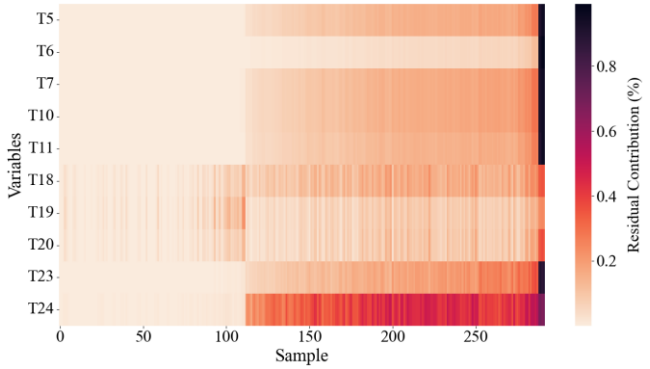

Figure 12. Distribution of feature residual contribution values for the Bearing1_1 dataset.

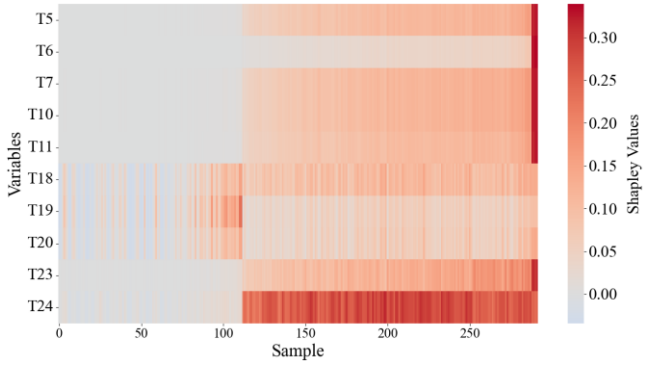

Figure 13. Distribution of feature Shapley values for the Bearing1_1 dataset.

The dataset Bearing1_1 is selected for analysis. First, the global quantitative contribution of features to all operating samples is examined. Based on Eq. 21, a two-dimensional matrix of instantaneous residual contribution rates is constructed and the corresponding heatmap is plotted, as shown in Figure 12. Simultaneously, a heatmap based on the Shapley values derived from MSET-SHAP is plotted, as shown in Figure 13. The comparison of these two heatmaps indicates a high consistency in the distribution trends of the presented indicators.

To further analyze the feature importance of MSET-SHAP under different operating conditions, SHAP feature importance plots for normal and abnormal states are presented in Figure 14. The horizontal axis represents the range of mean absolute Shapley values, while the vertical axis shows the names of the input features. A larger mean absolute Shapley value indicates a greater marginal contribution of the feature to the predicted residuals. From Figure 14, it can be observed that feature $t19$ has the most significant marginal contribution in the normal state, whereas feature $t24$ dominates in the abnormal state. Moreover, due to the drastic changes in feature values during the abnormal state, these variations substantially influence the model predictions, resulting in larger Shapley values for related features. Consequently, the mean absolute Shapley values of features in Figure 14(b) for the abnormal state are nearly an order of magnitude greater than those in Figure 14(a) for the normal state.

This study quantifies the marginal contribution rates by normalizing the mean absolute Shapley values, enabling a direct comparative analysis of the results obtained from two interpretability methods. The comparison results are presented in Figure 15. Under normal operating conditions, both methods consistently identify features $t24$, $t18$, $t19$, $t20$, and $t23$ as important. In abnormal conditions, the ranking of feature importance based on the cumulative contribution rate perfectly aligns with that of the marginal contribution rate. This finding provides dual validation for precise anomaly parameter localization and confirms the feasibility of the proposed method for interpretable anomaly parameter analysis.

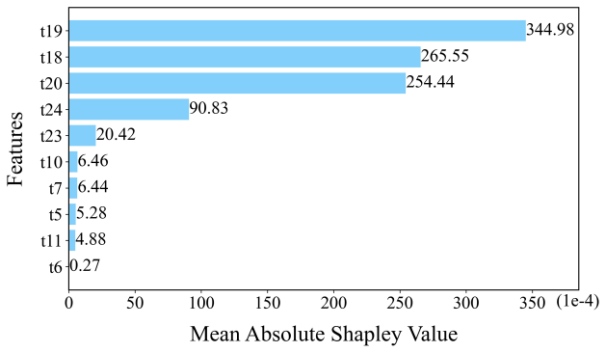

(a) Shapley Feature Importance under Normal Condition

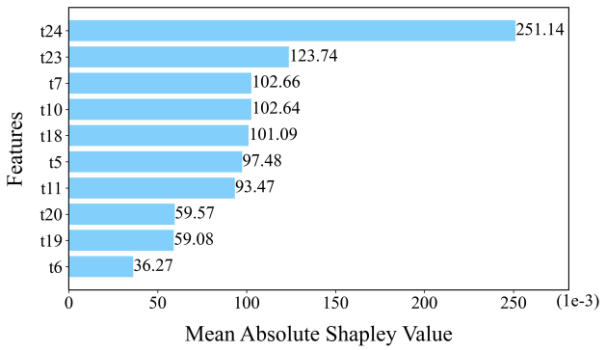

(b) Shapley Feature Importance under Faulty Condition

Figure 14. Shapley feature importance map.

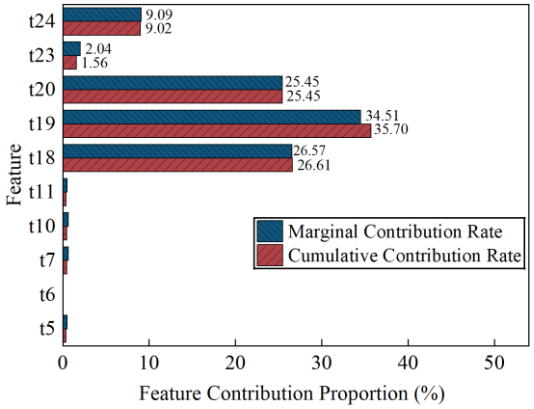

(a) Comparison of Explainability Methods under Normal Condition

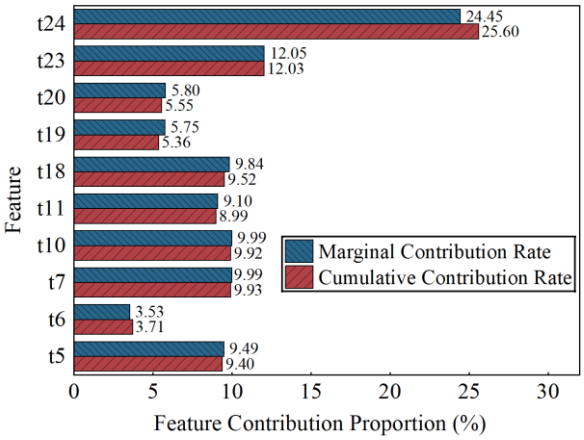

(b) Comparison of Explainability Methods under Faulty Condition

Figure 15. Comparison chart of interpretable methods.

The differences in explanatory mechanisms between the two methods lead to subtle discrepancies in feature importance metrics. The KernelSHAP method approximates the marginal contribution of each feature to the model prediction through kernel-weighted sampling, involving a relatively complex calculation that is highly dependent on the sampling strategy. Its computational complexity grows exponentially with the number of features. For the Bearing1_1 test dataset, the average inference time per sample using KernelSHAP is 4123.288 ms. Moreover, in the presence of complex interactions among features, KernelSHAP estimates are prone to bias. In contrast, the cumulative contribution rate interpretability method is computationally more efficient and straightforward, with an average inference time of 0.256 ms per sample. This method ranks features directly based on their cumulative contribution metrics, facilitating mechanistic interpretation and result explanation, while enabling rapid and accurate identification of key anomalous features. Consequently, it is well suited for real-time industrial fault diagnosis applications.

6. Conclusion

This study proposes an explainable, adaptive anomaly detection method for rotating machinery under multiple working conditions, combining Weighted Nearest Neighbor MSET and SPRT. The approach achieves high accuracy and precise localization of anomalies.

(1) Constructing the spatial MM by optimizing monitoring parameters with sensitivity and conflict indicators, alongside using improved KNN and K-means algorithms, effectively reduces computational complexity and enhances operational efficiency in multi-condition scenarios.

(2) A multiparameter anomaly detection method integrating MSET and SPRT is developed. Comparative evaluations show that the method achieves outstanding performance, with an average accuracy of 97.47% on multi-condition datasets.

(3) Based on feature cumulative contribution rates, an interpretability analysis of abnormal parameters was

conducted from multiple perspectives, including operating states, working conditions, and fault types, and compared with MSET-SHAP results. The findings show consistency between the two methods, with the proposed method offering a more intuitive and efficient process for fault traceability, supporting safe machinery operation in intelligent manufacturing.

However, several potential issues still warrant further investigation. First, the dependency of model interpretability on the quality of feature extraction has not been thoroughly examined. Second, the causal relationships among parameters and the underlying fault evolution mechanisms remain largely unexplored. These limitations constrain the explanatory power of the proposed interpretability framework. Beyond the cumulative abnormal contribution rate (CACR) and SHAP methods employed in this study, future work could integrate advanced techniques, such as graph neural networks and causal inference, to more comprehensively uncover the intrinsic relationships among feature parameters and latent fault mechanisms. Such efforts are expected to further enhance both the interpretability and practical applicability of the proposed model.

Acknowledgements

This work was supported by the National Key Research and Development Program of China(Grant Number: 2024YFB3409303).

References

1. An J, Liu J, Zhen H, Lu M. Camera-based PHM method in rotating machinery equipment micro-action scenarios. Eksploatacja i Niezawodność – Maintenance and Reliability 2023; 25(1): 10. https://doi.org/10.17531/ein.2023.1.10.
2. Zhang J, Kong X, Cheng L, Qi H, Yu M. Intelligent fault diagnosis of rolling bearings based on continuous wavelet transform-multiscale feature fusion and improved channel attention mechanism. Eksploatacja i Niezawodność – Maintenance and Reliability 2023; 25(1): 16. https://doi.org/10.17531/ein.2023.1.16.
3. Wei L, Peng X, Cao Y. Multi-scale graph transformer for rolling bearing fault diagnosis. Eksploatacja i Niezawodność – Maintenance and Reliability 2025; 27(2): 194779. https://doi.org/10.17531/ein/194779.
4. Lei C, Miao C, Yu Y, Wang L, Wang B. Rolling bearing fault diagnosis method based on multi-scale pooling residual convolutional neural network under noisy environment. Eksploatacja i Niezawodność – Maintenance and Reliability 2024; 27(1): 192167. https://doi.org/10.17531/ein/192167.
5. Wang J, Abdullah S, Arifin A, Karam Singh S S, Gao C. A semi-supervised fault diagnosis method for rolling bearing using time-frequency transform enhanced contrastive learning. Eksploatacja i Niezawodność – Maintenance and Reliability 2026; 28(1): 207015. https://doi.org/10.17531/ein/207015.
6. Bai R, Wang H, Sun W, Shi Y. Fault diagnosis method for rotating machinery based on SEDenseNet and gramian angular field. Eksploatacja i Niezawodność – Maintenance and Reliability 2024; 26(4): 1–17. https://doi.org/10.17531/ein/191445.
7. Wang X, Yao Y, Gao C. Wasserstein distance- EEMD enhanced multi-head graph attention network for rolling bearing fault diagnosis under different working conditions. Eksploatacja i Niezawodność – Maintenance and Reliability 2024; 26(2): 184037. https://doi.org/10.17531/ein/184037.
8. Zhang K, Yang G, Yang M, Ma C, Xu Y. LSESgram: a novel approach for optimal demodulation band selection in rolling bearing fault diagnosis. Eksploatacja i Niezawodność – Maintenance and Reliability 2026; 28(1): 208154. https://doi.org/10.17531/ein/208154.
9. Oshida T, Murakoshi T, Zhou L, Ojima H, Kaneko K, Onuki T, Shimizu J. Development and implementation of real-time anomaly detection on tool wear based on stacked LSTM encoder-decoder model. The International Journal of Advanced Manufacturing Technology 2023; 127(1-2): 263–278. https://doi.org/10.1007/s00170-023-11497-9.
10. Wang Y, Peng Y, Zi Y, Jin X, Tsui K-L. A two-stage data-driven-based prognostic approach for bearing degradation problem. IEEE Transactions on Industrial Informatics 2016; 12(3): 924–932. https://doi.org/10.1109/TII.2016.2535368.
11. Hardin J, Rocke D M. Outlier detection in the multiple cluster setting using the minimum covariance determinant estimator. Computational Statistics & Data Analysis 2004; 44(4): 625–638. https://doi.org/10.1016/S0167-9473(02)00280-3.
12. Wang Z, Jin X, Xu Z. An adaptive condition monitoring method of wind turbines based on multivariate state estimation technique and continual learning. IEEE Transactions on Instrumentation and Measurement 2023; 72: 1–9. https://doi.org/10.1109/TIM.2023.3265118.

13. Guo R, Zhang G, Zhang Q, Zhou L, Yu H, Lei M, Lv Y. An adaptive early fault detection model of induced draft fans based on multivariate state estimation technique. Energies 2021; 14(16): 4787. https://doi.org/10.3390/en14164787.
14. Caesarendra W, Tjahjowidodo T, Kosasih B, Tieu A K. Integrated condition monitoring and prognosis method for incipient defect detection and remaining life prediction of low speed slew bearings. Machines 2017; 5(2): 11–30. https://doi.org/10.3390/machines5020011.
15. Shan L, Liu Y, Ai X, Gao J. Research on fault sensor detection and localization method based on autoencoder. Annals of Nuclear Energy 2025; 220: 111546. https://doi.org/10.1016/j.anucene.2025.111546.
16. Yang K, Hu B, Malekian R, Li Z. An improved control-limit-based principal component analysis method for condition monitoring of marine turbine generators. Journal of Marine Engineering & Technology 2020; 19(4): 249–256. https://doi.org/10.1080/20464177.2019.1655135.
17. Saari J, Strömbergsson D, Lundberg J, Thomson A. Detection and identification of windmill bearing faults using a one-class support vector machine (SVM). Measurement 2019; 137: 287–301. https://doi.org/10.1016/j.measurement.2019.01.020.
18. Wang J, Kou M, Li R, Qian Y, Li Z. Ultra-short-term wind power forecasting jointly driven by anomaly detection, clustering and graph convolutional recurrent neural networks. Advanced Engineering Informatics 2025; 65: 103137. https://doi.org/10.1016/j.aei.2025.103137.
19. Cui L, Zhang Q, Shi Y, Yang L, Wang Y, Wang J, Bai C. A method for satellite time series anomaly detection based on fast-DTW and improved-KNN. Chinese Journal of Aeronautics 2023; 36(2): 149–159. https://doi.org/10.1016/j.cja.2022.05.001.
20. Wang H, Yang S, Liu Y, Li Q. A novel abnormal data detection method based on dynamic adaptive local outlier factor for the vibration signals of rotating parts. Measurement Science and Technology 2023; 34(8): 085118. https://doi.org/10.1088/1361-6501/accbda.
21. Shu X, Zhang S, Li Y, Chen M. An anomaly detection method based on random convolutional kernel andisolation forest for equipment state monitoring. Eksploatacja i Niezawodność – Maintenance and Reliability 2022; 24(4): 758–770. https://doi.org/10.17531/ein.2022.4.16.
22. Özüpak Y, Mansurov S. Optimizing electricity demand forecasting with a novel RNN-LSTM hybrid model. Energy Sources, Part B: Economics, Planning, and Policy 2025; 20(1): 2531448. https://doi.org/10.1080/15567249.2025.2531448.
23. Li E, Li Y, Bedi S, Melek W, Gray P. Incremental learning of LSTM-autoencoder anomaly detection in three-axis CNC machines. The International Journal of Advanced Manufacturing Technology 2024; 130(3-4): 1265–1277. https://doi.org/10.1007/s00170-023-12713-2.
24. Li X, Huang T, Cheng K, Qiu Z, Sichao T. Research on anomaly detection method of nuclear power plant operation state based on unsupervised deep generative model. Annals of Nuclear Energy 2022; 167: 108785. https://doi.org/10.1016/j.anucene.2021.108785.
25. He S, Xu X, Xie J, Wang F, Liu Z, Zhao F. Fault detection and fault-tolerant control of autonomous steering system for intelligent vehicles combining Bi-LSTM and SPRT. Measurement 2023; 212: 112708. https://doi.org/10.1016/j.measurement.2023.112708.
26. Wang B, Lei Y, Li N, Li N. A hybrid prognostics approach for estimating remaining useful life of rolling element bearings. IEEE Transactions on Reliability 2020; 69(1): 401–412. https://doi.org/10.1109/TR.2018.2882682.
27. Aslan E, Özüpak Y, Alpsalaz F, Elbarbary Z M S. A hybrid machine learning approach for predicting power transformer failures using internet of things-based monitoring and explainable artificial intelligence. IEEE Access 2025; 13: 113618–113633. https://doi.org/10.1109/ACCESS.2025.3583773.
28. Samee N A, Alhussan A A, Ghoneim V F, Atteia G, Alkanhel R, Al-antari M A, Kadah Y M. A hybrid deep transfer learning of CNN-based LR-PCA for breast lesion diagnosis via medical breast mammograms. Sensors 2022; 22(13): 4938. https://doi.org/10.3390/s22134938.
29. Nectoux P, Gouriveau R, Medjaher K, Ramasso E, Chebel-Morello B, Zerhouni N, Varnier C. PRONOSTIA: an experimental platform for bearings accelerated degradation tests. Conference on Prognostics and Health Management., Denver, Colorado, United States, IEEE Catalog Number : CPF12PHM-CDR: 2012;sur CD ROM:1–8.
30. Alpsalaz F. Fault detection in power transmission lines: comparison of chirp-Z algorithm and machine learning based prediction models. Eksploatacja i Niezawodność – Maintenance and Reliability 2025; 27(4): 14. https://doi.org/10.17531/ein/203949.
31. Aslan E. Temperature prediction and performance comparison of permanent magnet synchronous motors using different machine learning techniques for early failure detection. Eksploatacja i Niezawodność – Maintenance and Reliability 2025; 27(1): 192164. https://doi.org/10.17531/ein/192164.